Imaging diffusive media using time-independent and time-harmonic sources: dependence of image quality on imaging algorithms, target volume, weight matrix, and view angles

Jenghwa Chang[1], Raphael Aronson[2], Harry L. Graber[3], Randall L. Barbour[1,3]

[1]Departments of Pathology,
[3]Department of Physiology and Biophysics
SUNY Health Science Center at Brooklyn
450 Clarkson Ave.
Brooklyn, NY 11203

[2]Bioimaging Sciences Corp.
64 Burnett Terrace
West Orange, NJ 07052

ABSTRACT

We present results examining the dependence of image quality for imaging in dense scattering media as influenced by the choice of parameters pertaining to the physical measurement and factors influencing the efficiency of the computation. The former includes the choice of the weight matrix as affected by the target volume, view angle, and source condition. The latter includes the density of the weight matrix and type of algorithm used. These were examined by solving a one-step linear perturbation equation derived from the transport equation using three different algorithms: POCS, CGD, and SART algorithms with constraints. The above were explored by evaluating four different, 3-D cylindrical phantom media: a homogeneous medium, and media containing a single black rod on the axis, a single black rod parallel to the axis, and thirteen black rods arrayed in the shape of an "X." Solutions to the forward problem were computed using Monte Carlo methods for an impulse source, from which was calculated time-independent and time-harmonic detector responses.

The influence of target volume on image quality and computational efficiency was studied by computing solutions to three types of reconstructions: 1) 3-D reconstruction, which considered each voxel individually, 2) 2-D reconstruction, which assumed that symmetry along the cylinder axis was known *a priori*, 3) 2-D limited reconstruction, which assumed that only those voxels in the plane of the detectors contribute information to the detector readings. The effect of view angle was explored by comparing computed images obtained from a single source, whose position was varied, as well as for the type of tomographic measurement scheme used (*i.e.*, radial scan vs. transaxial scan). The former condition was also examined for the dependence of the above on choice of source condition (*i.e.*, cw (2-D reconstructions) vs. time-harmonic (2-D limited reconstructions) source).

The efficiency of the computational effort was explored, principally, by conducting a weight matrix "threshold titration" study. This involved computing the ratio of each matrix element to the maximum element of its row and setting this to zero if the ratio was less than a preselected threshold.

Results obtained showed that all three types of reconstructions provided good image quality. The 3-D reconstruction outperformed the other two reconstructions. The time required for 2-D and 2-D limited reconstruction is much less (< 10 %) than that for the 3-D reconstruction. The "threshold titration" study shows that artifacts were present when the threshold was 5% or higher, and no significant differences of image quality were observed when the thresholds were less than 1%, in which case 38% (21,849 of 57,600) of the total weight elements were set to zero. Restricting the view angle produced degradation in image quality, but, in all cases, clearly recognizable images were obtained.

1. INTRODUCTION

Our use of perturbation theory for optical diffusion tomography [1-3] involves solving a system of linear equations derived from the transport equation. The coefficients of the linear equations, the weight functions, which are determined

by the properties of the reference medium and the source-detector configuration, contain the essential information which will determine the achievable image quality. In general, the more measurement data available the better image quality is expected. However, because computing resources are limited, for example, by CPU time and memory, it is important to obtain an optimal balance between the amount of data being analyzed and the computing efficiency. The latter can be influenced by, for example, the number of unknowns, sparseness of the weight matrix and its size. Because the weight function relates the detectablity of different volumes for a specified source condition, proper selection of the source-detector configuration and view angle will be important in defining a scheme that optimizes the spatial information content of the measured data while minimizing the computing effort. The purpose of this study is to examine this relationship as influenced by the choice of the imaging algorithm, target volume, density of weight matrix, view angle, and source condition.

2. THEORY

The migration of monoenergetic photons through the medium can be described by the transport equation [4, 5]:

$$\frac{1}{c(\mathbf{r})}\frac{\partial \phi(\mathbf{r},\Omega,t)}{\partial t} + \Omega \cdot \nabla \phi(\mathbf{r},\Omega,t) + \mu_T(\mathbf{r},\Omega)\phi(\mathbf{r},\Omega,t) - \int \mu_s(\mathbf{r},\Omega'\cdot\Omega)\phi(\mathbf{r},\Omega',t)d\Omega' = s(\mathbf{r},\Omega,t), \tag{1}$$

where:

$c(\mathbf{r})$ = speed of light at $\mathbf{r}$ [length / time],

$d\Omega$ = differential solid angle,

Ω = unit vector in direction Ω,

$\phi(\mathbf{r},\Omega,t)$ = photon angular intensity at $\mathbf{r}$ with direction Ω [photons / area / solid angle / time],

$s(\mathbf{r},\Omega,t)$ = angular source density at $\mathbf{r}$ with direction Ω [photons / volume / solid angle / time],

$\mu_s(\mathbf{r},\Omega'\cdot\Omega)$ = macroscopic angular scattering cross section at $\mathbf{r}$ from direction Ω' into
    direction Ω [1 / length / solid angle],

$\mu_s(\mathbf{r},\Omega) = \int_{4\pi} \mu_s(\mathbf{r},\Omega\cdot\Omega')d\Omega'$ = macroscopic angular scattering cross section [1 / length],

$\mu_a(\mathbf{r},\Omega)$ = macroscopic angular absorption cross section [1 / length],

$\mu_T(\mathbf{r},\Omega) = \mu_a(\mathbf{r},\Omega) + \mu_s(\mathbf{r},\Omega)$ = macroscopic angular total cross section [1 / length].

Symbolically:

$$L\phi = s, \tag{2}$$

where L is an integrodifferential operator with kernel:

$$L(\mathbf{r},\Omega,\Omega',t) = \delta(\Omega - \Omega')\left[\frac{1}{c(\mathbf{r})}\frac{\partial}{\partial t} + \Omega \cdot \nabla + \mu_T(\mathbf{r},\Omega)\right] - \mu_s(\mathbf{r},\Omega'\cdot\Omega),$$

and:

$$\int L(\mathbf{r},\Omega,\Omega',t)\phi(\mathbf{r},\Omega',t)d\Omega' = s(\mathbf{r},\Omega,t).$$

The solution can be written symbolically as:

$$\phi = L^{-1}s. \tag{3}$$

The inverse, L^{-1}, that satisfies the boundary conditions is the Green's function. Thus, the solution is:

$$\phi(\mathbf{r},\Omega,t) = \int G(\mathbf{r},\Omega;\mathbf{r}',\Omega';t) \otimes s(\mathbf{r}',\Omega';t)d^3rd\Omega', \tag{4}$$

where $\otimes$ is the notation for time convolution. Now suppose that with the same source and boundary conditions, a change is made in the cross sections. We can write $L \to L + \Delta L$. As a result, the solution ϕ changes so that $\phi \to \phi + \Delta\phi$. Then:

$$(L + \Delta L)(\phi + \Delta\phi) = s,$$
$$L\Delta\phi + \Delta L\phi = s - L\phi - \Delta L\Delta\phi = -\Delta L\Delta\phi,$$
(5)

which is second-order in the change. For small changes it can be ignored, so:

$$L\Delta\phi = -\Delta L\phi,$$
(6)

and

$$\Delta\phi = -L^{-1}(\Delta L\phi).$$
(7)

That is, if ϕ is the solution satisfying the boundary conditions with source s, then $\Delta\phi$ is the solution satisfying the boundary conditions with source:

$$q = -\Delta L\phi.$$
$$\Delta\phi = L^{-1}q.$$
(8)

or, applying the transport operator L and its inverse L^{-1}:

$$q(\mathbf{r}, \Omega, t) = -\Delta\mu_T(\mathbf{r}, \Omega)\phi(\mathbf{r}, \Omega, t) + \int \Delta\mu_s(\mathbf{r}, \Omega' \cdot \Omega)\phi(\mathbf{r}, \Omega', t)d\Omega.$$
$$\Delta\phi(\mathbf{r}, \Omega, t) = \int G(\mathbf{r}, \Omega; \mathbf{r}', \Omega'; t)q(\mathbf{r}', \Omega', t)d^3r d\Omega'.$$
(9)

Let the response of a detector be a function of ϕ:

$$R(t) = (r, \phi) = \int r(\mathbf{r}, \Omega, t) \otimes \phi(r, \Omega, t)d^3r d\Omega$$
(10)

where $r(\mathbf{r}, \Omega, t)$ is the detector response function. Applying a well known reciprocity theory, Eq. (10) becomes

$$R(t) = (r, \phi) = (r, L^{-1}s) = \int r(\mathbf{r}, \Omega, t) \otimes \left(\int G(\mathbf{r}, \Omega; \mathbf{r}', \Omega'; t) \otimes s(\mathbf{r}', \Omega', t)d^3r' d\Omega'\right)d^3r d\Omega$$
$$= \int s(r, \Omega, t) \otimes \left(\int G(\mathbf{r}, -\Omega; \mathbf{r}', -\Omega'; t) \otimes r(\mathbf{r}', \Omega', t)d^3r' d\Omega'\right)d^3r d\Omega = (L^{-1+}r, s) = (\phi^+, s)$$
(11)

where L^{-1+} is the adjoint of L^{-1}, and

$$\phi^+(\mathbf{r}, \Omega, t) = \int G(\mathbf{r}, -\Omega; \mathbf{r}', -\Omega'; t) \otimes r(\mathbf{r}', \Omega', t)d^3r' d\Omega'$$

is the adjoint solution. The physical meaning of $\phi^+(\mathbf{r}, \Omega, t)$ can be interpreted as the forward solution at $\mathbf{r}$ with direction $-\Omega$ satisfying the boundary conditions with source $r(\mathbf{r}, -\Omega, t)$. The change in R due to the change in cross sections is given by:

$$\Delta R(t) = (\phi^+, q) = \int \phi^+(\mathbf{r}, \Omega, t) \otimes \left[\int \Delta\mu_s(\mathbf{r}, \Omega' \cdot \Omega)\phi(\mathbf{r}, \Omega', t)d\Omega' - \Delta\mu_T(\mathbf{r}, \Omega)\phi(\mathbf{r}, \Omega, t)\right]d^3r d\Omega$$
(12)

Let us evaluate $\Delta R(t)$ of Eq. (12) in terms of a spherical harmonic expansion. We choose to use the unnormalized real spherical harmonics as the basis functions:

$$Y_{ml}^e(\Omega) \equiv Y_{ml}^e(\theta,\varphi) = P_l^m(\cos\theta)\cos m\varphi, \qquad 0 \le m \le l,$$
$$Y_{ml}^o(\Omega) \equiv Y_{ml}^o(\theta,\varphi) = P_l^m(\cos\theta)\sin m\varphi, \qquad 1 \le m \le l, \tag{13}$$

where $\Omega = (\theta,\varphi)$, θ and φ are the polar angle and azimuth, respectively, and the P_l^m are the associated Legendre functions. The orthogonality conditions are given by:

$$\int Y_{ml}^\alpha(\Omega) Y_{m'l'}^\beta(\Omega)\, d\Omega = \frac{4\pi}{(2l+1)\varepsilon_m}\frac{(l+m)!}{(l-m)!}\delta_{ll'}\delta_{mm'}\delta_{\alpha\beta}, \quad \varepsilon_m = \begin{cases} 1, & m=0 \\ 2, & m>0 \end{cases} \tag{14}$$

Here, α and β can take on the values e and o. Thus we expand the direct and adjoint intensity:

$$\phi(\mathbf{r},\Omega,t) = \sum_{l=0}^\infty \sum_{m=0}^l \sum_{\alpha=e,o} a_{lm}^\alpha(\mathbf{r},t) Y_{ml}^\alpha(\Omega), \qquad \phi^+(\mathbf{r},\Omega,t) = \sum_{l=0}^\infty \sum_{m=0}^l \sum_{\alpha=e,o} a_{lm}^{+\alpha}(\mathbf{r},t) Y_{ml}^\alpha(\Omega). \tag{15}$$

where, $a_{lm}^\alpha(\mathbf{r},t)$ and $a_{lm}^{+\alpha}(\mathbf{r},t)$ are the expansion coefficients. Note that $Y_{0l}^o(\Omega) = 0$. From Eq. (12)

$$\int \phi(\mathbf{r},\Omega,t) \otimes \phi^+(\mathbf{r},\Omega,t) d\Omega = \sum_{l,m,\alpha}\sum_{l',m',\beta} a_{lm}^\alpha(\mathbf{r},t) \otimes a_{l'm'}^{+\beta}(\mathbf{r},t)\int Y_{ml}^\alpha(\Omega) Y_{m'l'}^\beta(\Omega) d\Omega = \sum_{l,m,\alpha}\frac{4\pi}{(2l+1)\varepsilon_m}\frac{(l+m)!}{(l-m)!} a_{lm}^\alpha(\mathbf{r}) a_{lm}^{+\alpha}(\mathbf{r}) \tag{16}$$

The differential cross section can be expanded in partial waves (i.e., Legendre polynomials) as:

$$\mu_s(\mathbf{r},\Omega'\cdot\Omega) = \mu_s(\mathbf{r})\sum_{l=0}^\infty \frac{2l+1}{4\pi} f_l P_l(\Omega'\cdot\Omega). \tag{17}$$

With this definition of the expansion coefficients, the normalization gives $f_0 = 1$. With this choice of basis functions and coefficients, f_l is the lth moment of the differential cross section. The addition theorem for spherical harmonics is:

$$P_l(\Omega'\cdot\Omega) = P_l(\cos\theta') P_l(\cos\theta) + 2\sum_{m=1}^l \frac{(l-m)!}{(l+m)!} P_m^l(\cos\theta') P_m^l(\cos\theta)\cos m(\varphi'-\varphi) = \sum_{m=1}^l \varepsilon_m \frac{(l-m)!}{(l+m)!}\sum_\alpha Y_{ml}^\alpha(\Omega') Y_{ml}^\alpha(\Omega). \tag{18}$$

Then:

$$\int P_l(\Omega'\cdot\Omega)\,\phi^+(\mathbf{r},\Omega',t) d\Omega' = \sum_{m,\alpha}\sum_{l',m',\beta}\varepsilon_m \frac{(l-m)!}{(l+m)!} a_{l'm'}^{+\beta}(\mathbf{r},t) Y_{ml}^\alpha(\Omega)\int Y_{ml}^\alpha(\Omega') Y_{ml}^\beta(\Omega') d\Omega' = \frac{4\pi}{2l+1}\sum_{m,\alpha} a_{lm}^{+\alpha}(\mathbf{r},t) Y_{ml}^\alpha(\Omega), \tag{19}$$

so:

$$\int \mu_s(\mathbf{r},\Omega'\cdot\Omega)\phi^+(\mathbf{r},\Omega',t) d\Omega' = \mu_s(\mathbf{r})\sum_{l,m,\alpha} f_l a_{lm}^{+\alpha}(\mathbf{r},t) Y_{ml}^\alpha(\Omega), \tag{20}$$

and:

$$\int \phi(\mathbf{r},\Omega,t) \otimes \left(\int \mu_s(\mathbf{r},\Omega'\cdot\Omega)\phi^+(\mathbf{r},\Omega',t) d\Omega'\right) d\Omega = \mu_s(\mathbf{r})\sum_{l,m,\alpha}\frac{4\pi}{(2l+1)\varepsilon_m}\frac{(l+m)!}{(l-m)!} f_l a_{lm}^\alpha(\mathbf{r},t) \otimes a_{lm}^{+\alpha}(\mathbf{r},t). \tag{21}$$

If $\mu_s(\mathbf{r},\Omega\cdot\Omega') \to \Delta\mu_s(\mathbf{r},\Omega\cdot\Omega')$ and $\mu_s(\mathbf{r})f_l \to \Delta[\mu_s(\mathbf{r})f_l]$. Thus:

$$\Delta R(t) = \int \sum_{l,m,\alpha} \frac{4\pi}{(2l+1)\varepsilon_m} \frac{(l+m)!}{(l-m)!} \Delta[\mu_s(\mathbf{r})f_l - \mu_T(\mathbf{r})] a_{lm}^\alpha(\mathbf{r},t) \otimes a_{lm}^{+\alpha}(\mathbf{r},t)\, d^3r. \tag{22}$$

At this point, we assume that the anisotropy of $\phi(\mathbf{r},\Omega,t)$ and $\phi^+(\mathbf{r},\Omega,t)$ is not too large, and that it is adequate to expand up to terms in $l = 1$. The truncation occurs in the expression for $\Delta R(t)$ only, not in the calculation of $\phi(\mathbf{r},\Omega,t)$ and $\phi^+(\mathbf{r},\Omega,t)$, which would be equivalent to diffusion theory. Thus,

$$\Delta R(t) \approx \int \Big[4\pi\Delta[\mu_s(\mathbf{r}) - \mu_T(\mathbf{r})] a_{00}^e(\mathbf{r},t) \otimes a_{00}^{+e}(\mathbf{r},t)$$

$$+ \frac{4\pi}{3} \Delta[\mu_s(\mathbf{r})f_1 - \mu_T(\mathbf{r})]\big(a_{10}^e(\mathbf{r},t) \otimes a_{10}^{+e}(\mathbf{r},t) + a_{11}^e(\mathbf{r},t) \otimes a_{11}^{+e}(\mathbf{r},t) + a_{11}^o(\mathbf{r},t) \otimes a_{11}^{+o}(\mathbf{r},t) \big) \Big] d^3r \tag{23}$$

Now, :

$$P_0^0(\mu) = 1, \quad P_1^0(\mu) = \mu, \quad P_1^1(\mu) = \sqrt{1 - \mu^2}.$$

Then:

$$Y_{00}^e(\Omega) = P_0^0(\cos\theta) = 1, \qquad\qquad Y_{01}^e(\Omega) = P_1^0(\cos\theta) = \cos\theta = \Omega\cdot\mathbf{k},$$

$$Y_{11}^e(\Omega) = P_1^1(\cos\theta)\cos\varphi = \sin\theta\cos\varphi = \Omega\cdot\mathbf{i}, \qquad Y_{11}^o(\Omega) = P_1^1(\cos\theta)\sin\varphi = \sin\theta\sin\varphi = \Omega\cdot\mathbf{j}.$$

and

$$a_{00}^e(\mathbf{r},t) = \frac{1}{4\pi}\int \phi(\mathbf{r},\Omega,t)d\Omega = \frac{1}{4\pi}\phi(\mathbf{r},t), \qquad a_{10}^e(\mathbf{r},t) = \frac{3}{4\pi}\int \phi(\mathbf{r},\Omega,t)\Omega\cdot\mathbf{k}\, d\Omega = \frac{3}{4\pi}J_z(\mathbf{r},t),$$

$$a_{11}^e(\mathbf{r},t) = \frac{3}{4\pi}\int \phi(\mathbf{r},\Omega,t)\Omega\cdot\mathbf{i}\, d\Omega = \frac{3}{4\pi}J_x(\mathbf{r},t), \qquad a_{11}^o(\mathbf{r},t) = \frac{3}{4\pi}\int \phi(\mathbf{r},\Omega,t)\Omega\cdot\mathbf{j}\, d\Omega = \frac{3}{4\pi}J_y(\mathbf{r},t).$$

Here, $\phi(\mathbf{r},t) = \int \phi(\mathbf{r},\Omega,t)d\Omega =$ total intensity, $\mathbf{J}(\mathbf{r},t) = \int \phi(\mathbf{r},\Omega,t)\Omega\, d\Omega =$ flux. The relation between the $a_{lm}^{+\alpha}(\mathbf{r},t)$ and $\phi^+(\mathbf{r},\Omega,t)$ is similar, but with a minor difference. That is, we define:

$$\phi^+(\mathbf{r},t) = \int \phi^+(\mathbf{r},-\Omega,t)d\Omega = \int \phi^+(\mathbf{r},\Omega,t)d\Omega, \quad \mathbf{J}^+(\mathbf{r},t) = \int \phi^+(\mathbf{r},-\Omega,t)\Omega d\Omega = -\int \phi^+(\mathbf{r},\Omega,t)\Omega d\Omega. \tag{24}$$

The reason for these definitions is that $\phi^+(\mathbf{r},-\Omega,t)$ is the forward solution at $\mathbf{r}$ with direction Ω satisfying the boundary conditions with source $r(\mathbf{r}',-\Omega',t)$. Thus:

$$a_{00}^{e+}(\mathbf{r},t) = \frac{1}{4\pi}\phi^+(\mathbf{r},t), \quad a_{10}^{e+}(\mathbf{r},t) = \frac{-3}{4\pi}J_z^+(\mathbf{r},t), \quad a_{11}^{e+}(\mathbf{r},t) = \frac{-3}{4\pi}J_x^+(\mathbf{r},t), \quad a_{11}^{o+}(\mathbf{r},t) = \frac{-3}{4\pi}J_y^+(\mathbf{r},t).$$

and

$$\Delta R(t) \approx \int \left[\frac{1}{4\pi} \Delta[\mu_s(\mathbf{r}) - \mu_T(\mathbf{r})]\phi(\mathbf{r},t) \otimes \phi^+(\mathbf{r},t) - \frac{3}{4\pi} \Delta[\mu_s(\mathbf{r})f_1 - \mu_T(\mathbf{r})] \mathbf{J}(\mathbf{r},t) \otimes \mathbf{J}^+(\mathbf{r},t) \right] d^3r$$

$$= \int \left[\frac{-1}{4\pi} \Delta\mu_a \phi(\mathbf{r},t) \otimes \phi^+(\mathbf{r},t) + \frac{3}{4\pi} \Delta\mu_{tr}(\mathbf{r}) \mathbf{J}(\mathbf{r},t) \otimes \mathbf{J}^+(\mathbf{r},t) \right] d^3r$$

$$= \int \left[\frac{-1}{4\pi} \Delta\mu_a(\mathbf{r})\left[\phi(\mathbf{r},t) \otimes \phi^+(\mathbf{r},t) - 3\mathbf{J}(\mathbf{r},t) \otimes \mathbf{J}^+(\mathbf{r},t)\right] + \frac{3(1-f_1)}{4\pi} \Delta\mu_s(\mathbf{r}) \mathbf{J}(\mathbf{r},t) \otimes \mathbf{J}^+(\mathbf{r},t) \right] d^3r$$

$$= \int \left[\Delta\mu_a(\mathbf{r}) w_a(\mathbf{r},t) + \Delta\mu_s(\mathbf{r}) w_s(\mathbf{r},t) \right] d^3r, \tag{25}$$

where $\mu_{tr} = \mu_T(\mathbf{r}) - f_1\mu_s(\mathbf{r})$, and $w_a(\mathbf{r},t)$ and $w_s(\mathbf{r},t)$ are the weight for $\mu_a(\mathbf{r})$ and $\mu_s(\mathbf{r})$. Table 1 summarizes the transport equation, the perturbation equation, and the approximate weight function using spherical harmonic expansion, for time-resolved (TR), time-harmonic (TH), and continuous-wave (CW) cases. TH is the Fourier transform of the TR, and CW is a special case of TH in which ω is set equal to zero. The above equation can be discretized and represented in matrix form as:

$$\Delta\mathbf{R} = \mathbf{W} \cdot \Delta\mu, \tag{26}$$

where

$$\Delta\mathbf{R} = \begin{bmatrix} \Delta R_1 \\ \Delta R_2 \\ \vdots \\ \Delta R_I \end{bmatrix}, \quad \mathbf{W} = \begin{bmatrix} \mathbf{w}_1 & \mathbf{w}_2 & \cdots & \mathbf{w}_{2J} \end{bmatrix} = \begin{bmatrix} w_{11} & w_{12} & \cdots & w_{1,2J} \\ w_{21} & w_{22} & \cdots & w_{2,2J} \\ \vdots & \vdots & \ddots & \vdots \\ w_{I1} & w_{I2} & \cdots & w_{I,2J} \end{bmatrix}, \quad \Delta\mu = \begin{bmatrix} \Delta\mu_{a1} \\ \vdots \\ \Delta\mu_{aJ} \\ \Delta\mu_{s1} \\ \vdots \\ \Delta\mu_{sj} \end{bmatrix}$$

where I is the total number of source-detector pairs and J is the total number of voxels.

3. METHODS

3.1 Simulation setup

Figures 1 and 2 illustrate the simulation setup for this study. Four different 3-D cylindrical, isotropically scattering media were modeled using Monte Carlo methods to compute the internal light distributions and the flux of light re-emitted across the surface. The computed internal intensity was then used for the calculation of weight function, and the re-emitted light for detector readings. In all cases, the model media examined were cylindrical in shape, infinitely long and 20 mean free pathlengths (mfp) in diameter. The light source was a pencil beam directed normally (Figure 1A) or obliquely (Figure 1B) to the surface. Each cross section was discretized along the longitudinal (ρ) and azimuthal (φ) axis to 400 voxels (Figure 1C). Detector readings were computed for detectors arrayed every 10° on the boundary of the plane containing the source beam and perpendicular to the cylinder axis (Figures 1 and 2). Four different media were used: a homogeneous phantom, used as the reference medium (Figure 2A), and media containing a single black rod 2 mfp in diameter on the axis (Figure 2B), a single black rod 2 mfp in diameter and positioned parallel to the axis (Figure 2C) and half way between the center and the edge, and thirteen black rods (each 0.5 mfp in diameter) arrayed in the shape of "X" (Figure 2D). A total of 2×10^8 photons were launched into the medium for the calculation of internal intensity and detector readings for the 13 rod case, and 5×10^7 photons for calculation of detector readings for the centered and off-axis cases.

Figure 3 illustrates the source configurations for image reconstruction. Four sources, located 90° apart on the boundary of the central plane ($z = 0$) of the cylinder, and normal to the boundary, were used for the centered rod or off-

Table 1.

	Transport Equation	Perturbation Equation	Approximate Weight Function
TR	$\dfrac{1}{c(\mathbf{r})}\dfrac{\partial\phi(\mathbf{r},\Omega,t)}{\partial t} + \Omega\cdot\nabla\phi(\mathbf{r},\Omega,t)$ $+\,\mu_T(\mathbf{r},\Omega)\phi(\mathbf{r},\Omega,t) - \int\mu_s(\mathbf{r},\Omega'\cdot\Omega)$ $\phi(\mathbf{r},\Omega',t)d\Omega' = s(\mathbf{r},\Omega,t)$	$\Delta R = \int\phi^+(\mathbf{r},\Omega,t)\otimes\left[\left[\int\Delta\mu_s(\mathbf{r},\Omega'\cdot\Omega)\phi(\mathbf{r},\Omega',t)d\Omega'\right]\right.$ $\left.-\Delta\mu_T(\mathbf{r},\Omega)\phi(\mathbf{r},\Omega,t)\right]d^3r\,d\Omega$	$w_a(\mathbf{r},t) = \dfrac{-1}{4\pi}\left[\begin{array}{c}\phi(\mathbf{r},t)\otimes\phi^+(\mathbf{r},t)\\ -3\mathbf{J}(\mathbf{r},t)\otimes\mathbf{J}^+(\mathbf{r},t)\end{array}\right]$, $w_s(\mathbf{r},t) = \dfrac{3(1-f_1)}{4\pi}\mathbf{J}(\mathbf{r},t)\otimes\mathbf{J}^+(\mathbf{r},t)$,
TH	$\dfrac{j\omega}{c(\mathbf{r})}\bar\phi(\mathbf{r},\Omega,\omega) + \Omega\cdot\nabla\bar\phi(\mathbf{r},\Omega,\omega)$ $+\,\mu_T(\mathbf{r},\Omega)\bar\phi(\mathbf{r},\Omega,\omega) - \int\mu_s(\mathbf{r},\Omega'\cdot\Omega)$ $\bar\phi(\mathbf{r},\Omega',\omega)d\Omega' = \bar s(\mathbf{r},\Omega,\omega)$,	$\Delta R = \int\bar\phi^+(\mathbf{r},\Omega,\omega)\left[\left[\int\Delta\mu_s(\mathbf{r},\Omega'\cdot\Omega)\bar\phi(\mathbf{r},\Omega,\omega)d\Omega'\right]\right.$ $\left.-\Delta\mu_T(\mathbf{r},\Omega)\bar\phi(\mathbf{r},\Omega,\omega)\right]d^3r\,d\Omega$	$w_a(\mathbf{r},\omega) = \dfrac{-1}{4\pi}\left[\begin{array}{c}\bar\phi(\mathbf{r},\omega)\bar\phi^+(\mathbf{r},\omega)\\ -3\bar{\mathbf{J}}(\mathbf{r},\omega)\cdot\bar{\mathbf{J}}^+(\mathbf{r},\omega)\end{array}\right]$, $w_s(\mathbf{r},\omega) = \dfrac{3(1-f_1)}{4\pi}\bar{\mathbf{J}}(\mathbf{r},\omega)\cdot\bar{\mathbf{J}}^+(\mathbf{r},\omega),$
CW	$\Omega\cdot\nabla\phi(\mathbf{r},\Omega) + \mu_T(\mathbf{r},\Omega)\phi(\mathbf{r},\Omega) -$ $\int\mu_s(\mathbf{r},\Omega'\cdot\Omega)\phi(\mathbf{r},\Omega')d\Omega = s(\mathbf{r},\Omega)$	$\Delta R = \int\phi^+(\mathbf{r},\Omega)\left[\left[\int\Delta\mu_s(\mathbf{r},\Omega'\cdot\Omega)\phi(\mathbf{r},\Omega)d\Omega'\right]\right.$ $\left.-\Delta\mu_T(\mathbf{r},\Omega)\phi(\mathbf{r},\Omega)\right]d^3r\,d\Omega$	$w_a(\mathbf{r}) = \dfrac{-1}{4\pi}\left[\phi(\mathbf{r})\phi^+(\mathbf{r}) - 3\mathbf{J}(\mathbf{r})\cdot\mathbf{J}^+(\mathbf{r})\right]$, $w_s(\mathbf{r}) = \dfrac{3(1-f_1)}{4\pi}\mathbf{J}(\mathbf{r})\cdot\mathbf{J}^+(\mathbf{r}),$

$\Delta R(t) = \int\left[\Delta\mu_a(\mathbf{r})\,w_a(\mathbf{r},t) + \Delta\mu_s(\mathbf{r})\,w_s(\mathbf{r},t)\right]d^3r$

$\bar\phi(\mathbf{r},\omega) = \mathcal{F}[\phi(\mathbf{r},t)]$,

$\phi(\mathbf{r},t) = \int\phi(\mathbf{r},\Omega,t)d\Omega$

$\bar{\mathbf{J}}(\mathbf{r},\omega) = \mathcal{F}[\mathbf{J}(\mathbf{r},t)]$,

$\mathbf{J}(\mathbf{r},t) = \int\phi(\mathbf{r},\Omega,t)\Omega\,d\Omega.$

$\mathcal{F}$: Fourier transform.

Table 1. Summary of the transport equations, the perturbation equations, and the approximations of the weight function using spherical harmonic expansion for time-resolved (TR), time-harmonic (TH), and continuous-wave (CW) cases.
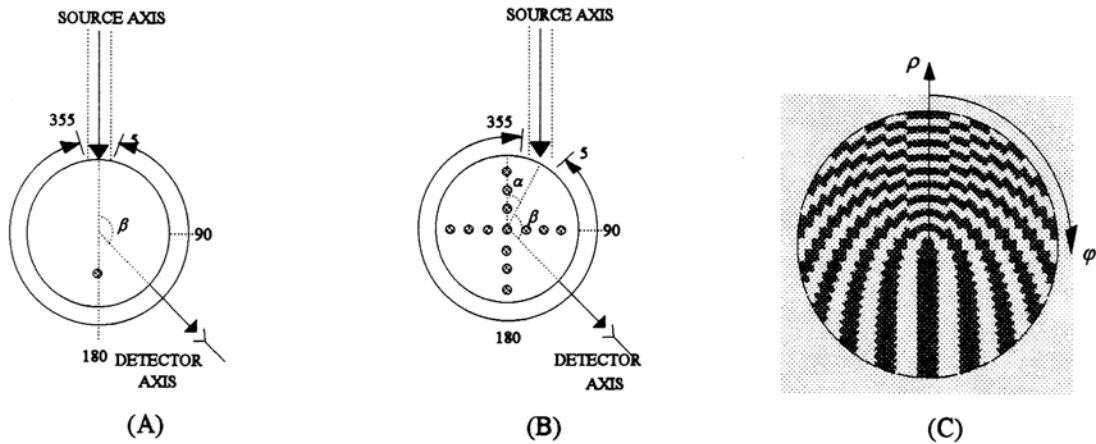
Figure 1. Sketch of illumination condition and grid geometries. Two types of source were used: (A) pencil beam normal to the surface, and (B) pencil beam oblique to the surface. Detectors were located every 10° on the boundary of the plane containing the source and perpendicular to the cylinder axis. (C) Each plane was discretized along the longitudinal and azimuthal axis to 400 voxels.
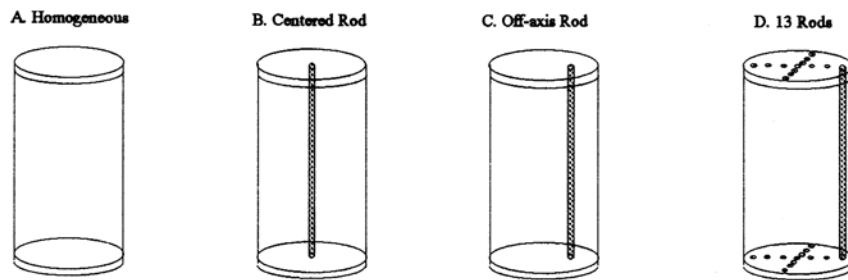

Figure 2. Tissue phantoms used for Monte Carlo simulations: (A) homogeneous phantom, used as the reference medium, (B) centered rod phantom containing a single black rod located on the axis, (C) off-axis rod phantom containing a single black rod located parallel to the axis, and (D) 13 rod phantom containing thirteen black rods located arrayed in the shape of "X."
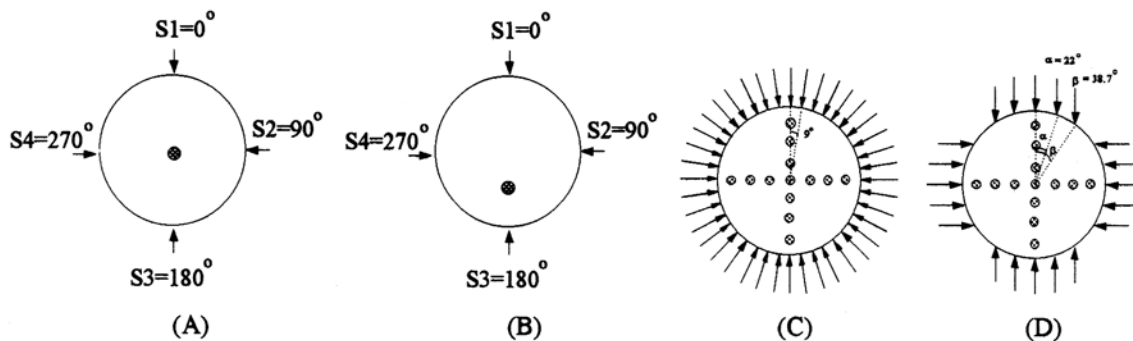
Figure 3. Source configurations used for image reconstruction for: (A) centered rod case, (B) off-axial rod case, (C) 13-rod case (normal), (D) 13-rod case (normal and oblique).

axial rod case (Figures 3A and 3B). Since each source has 36 detectors, 144 source-detector pairs were used for these two cases. Two source configurations were adopted for the 13 rod case. The first one (Figure 3C) used 40 sources (thus 1440 source-detector pairs) which were positioned every 9° about the cylinder and were normal to the boundary. The second one employed 16 oblique sources, and four normal sources (Figure 3D). The detectors of the normal and oblique sources are uncollimated. Totally, 720 source-detector pairs were considered.

3.2 Reconstruction Algorithms

Three reconstruction algorithms - projection onto convex sets (POCS) [6], conjugate gradient descent (CGD) [7, 8] method, and simultaneous algebraic reconstruction technique (SART) [9, 10] were used to solve Eq. (26) for image reconstruction:

POCS

$$\Delta\mu^{n+1} = P_L \circ P_{L-1} \circ \ldots \circ P_1 \Delta\mu^n$$

CGD

$$g^0 = A \cdot \Delta\mu_a^0 - b, \quad \beta^1 = 0, \quad d^1 = -g^0,$$

$$\beta^n = \frac{\|g^{n-1}\|^2}{\|g^{n-2}\|^2}, \quad d^n = -g^{n-1} + \beta^n d^{n-1},$$

$$\alpha^n = \frac{g^{n-1^T} \cdot g^{n-1}}{d^{n^T} \cdot A \cdot d^n}, \quad \Delta\mu^n = \Delta\mu^{n-1} - \alpha^n d^n,$$

$$g^n = A \cdot \Delta\mu_a^n - b = g^{n-1} - \alpha^n \cdot A \cdot d^n.$$

SART

$$\Delta\mu_j^{n+1} = \Delta\mu_j^n + \frac{\sum_{i=1}^{I} w_{ij} \frac{\Delta R_i - \sum_{j=1}^{2J} w_{ij}\Delta\mu_j^n}{\sum_{j=1}^{2J} w_{ij}}}{\sum_{i=1}^{I} w_{ij}}$$

where in POCS, P_i is the i-th constraint set, and " $\circ$ " is the projection onto each constraint set, and in CGD, $A = W^T \cdot W$ and $b = W \cdot \Delta R$.

Positivity constraints were applied to both detector reading and reconstructed results. Range constraints on the detector readings were imposed prior to reconstruction, with all the negative readings set to zero. The range constraints on reconstruction results were imposed after each iteration, with all the negative reconstructed results set to zero. A developed divergence detection scheme [11] were used while applying positivity constraints in the CGD algorithm. Three rescaling techniques [11] - (1) no rescaling; (2) rescaling the maximum of each column to 1; and (3) rescaling the average of each column to 1, were also used. For details of the constrained CGD and rescaling techniques, see [11]

3.3 Reconstruction types

The whole 3-D volume considered in the study was the cylinder extended from $z = -5$ to $z = 5$. Three types of reconstruction were computed: (1) 3–D reconstruction which considered each voxel individually, as shown in Figure 4A, (2) 2–D reconstruction (Figure 4B), which assumed that symmetry in the z direction was known *a priori*, (3) 2–D limited reconstruction (Figure 4C), which assumed that only those voxels in the central plane ($z = 0$) contribute information to the detector readings. Totally, 4400 unknowns were used for 3-D reconstruction, and 400 for 2-D and 2-D limited reconstructions.
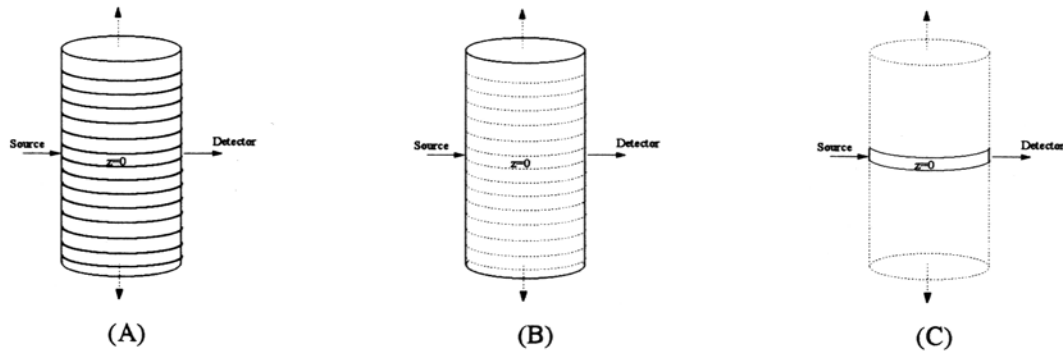
Figure 4. Three types of reconstruction: (A) 3-D Reconstruction; (B) 2-D Reconstruction; (3) 2-D Limited Reconstruction.

3.4 Weight threshold titration study

In this study we examined the influence of "sparseness" of the weight matrix on image quality. This was accomplished by setting increasing numbers of non-zero weight elements to zero and comparing the resultant image quality. The weight matrix corresponding to the 2-D reconstruction type was used for this study. The steps are listed as follows:

1. Set a cutoff value.
2. Calculate the ratio of each matrix element to the maximum element of its row.
3. Set the element to zero if the ratio was less than the cutoff.
4. Reconstruct images
5. Go to step 1 for next cutoff.

Five cutoff values: 10.0%, 5.0%, 1.0%, 0.5%, and 0.1%, were used. Reconstruction were performed using all three algorithms with rescaling technique and positivity constraints.

3.5 View angle study

Two view angle studies were performed using the three algorithms with the rescaling technique and positivity constraints. The first used only the detector readings from each source shown in Figure 3B to reconstruct images for the off-axis rod case, instead of using all four sources. CW sources were used for 2-D reconstruction using the three algorithms. 2-D limited reconstructions using TH sources were also performed using CGD method. The detector readings and internal intensity values were obtained by Fourier transforming the simulated TR data. Table 2 lists the selected frequencies for this study. These were obtained by assuming 1 mft equals 5 picoseconds. The width of the simulated impulse response is, in all cases, less than 500 mft and depended on the source and detector position. Also listed in Table 2 is the corresponding period in mft.

The second study incorporated detector readings from both normal and oblique sources, as shown in Figure 3D, for the 13 rod case. Four normal sources and 16 oblique sources were used for the 2-D reconstructions.
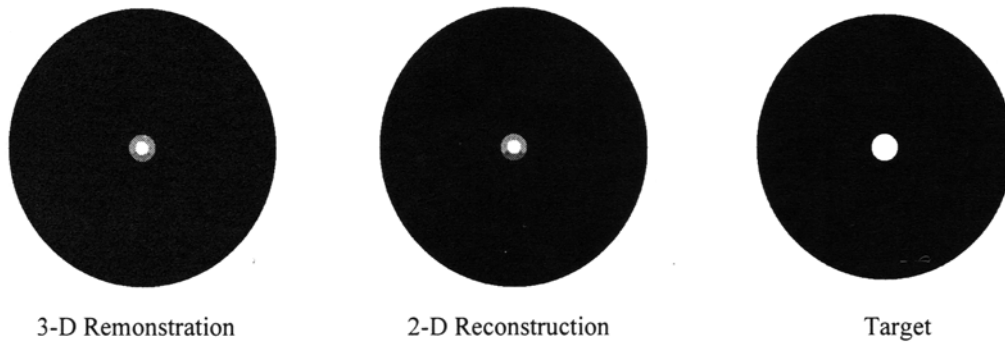
Table 2.

Frequency (Hz):	DC	100 MHz	1 GHz	10 GHz
Frequency (mft^{-1}):	DC	5×10^{-4} mft^{-1}	5×10^{-3} mft^{-1}	5×10^{-2} mft^{-1}
Period (mft):	∞	2×10^{3} mft	200 mft	20 mft

List of frequencies in Hz, frequencies in mft^{-1}, and period in mft used for the view angle study.
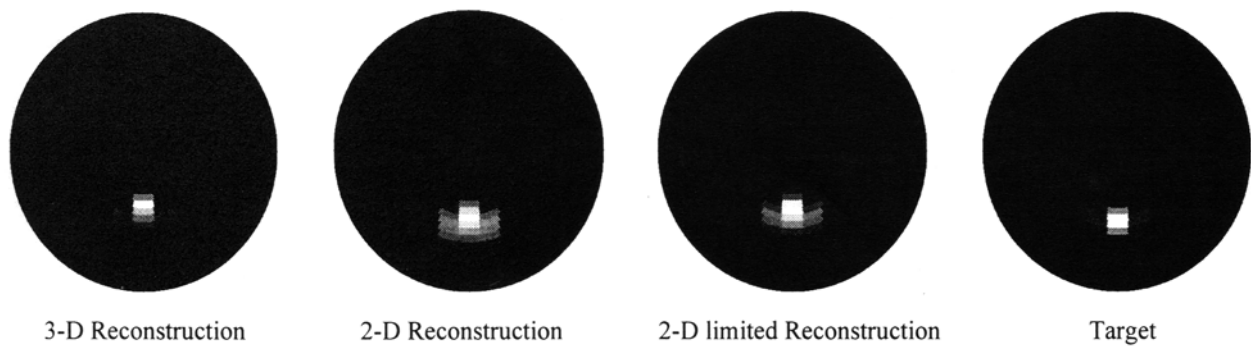
4. RESULTS

Figure 5 shows the 3-D and 2-D CW reconstruction results using the SART algorithm and rescaling technique (rescaling the maximum value of each column vector to 1) for the centered rod, off-axis rod, and 13 rod cases after 1,000, 10,000, and 1,000 iterations, respectively. A 2-D limited reconstruction is also shown for the off-axis rod case after 10,000

(A) Centered rod case

3-D Remonstration   2-D Reconstruction   Target

(B) Off-axis rod case

3-D Reconstruction   2-D Reconstruction   2-D limited Reconstruction   Target

(C) 13 rod case

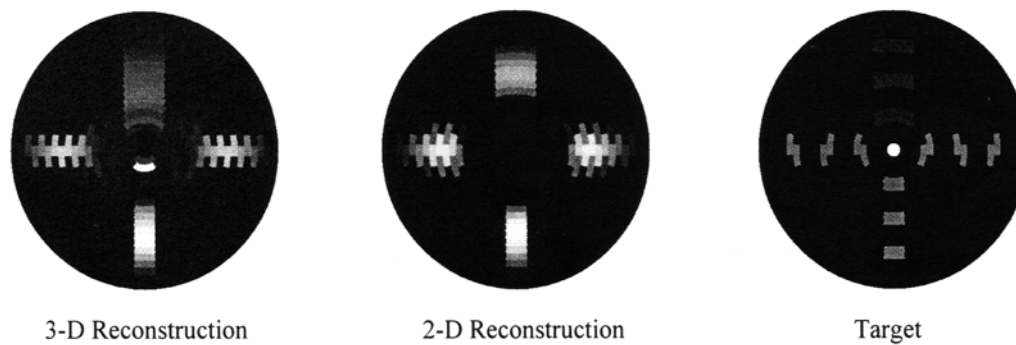3-D Reconstruction   2-D Reconstruction   Target

Figure 5. 3-D, 2-D, and 2-D limited reconstruction results using the SART algorithm and rescaling technique by rescaling the maximum of each column vector to 1, for (A) centered rod case after 1,000 iterations, (B) off-center rod case after 10,000 iterations, and (C) 13 rod case after 1,000 iterations. The radial illumination scheme as shown in Figure 3C was employed.

iterations. Table 3 lists the number of weight elements set to 0 in the titration study using three different rescaling techniques: (1) rescaling the maximum value of the weight element in each column vector to 1, (2) rescaling the average of each column vector to 1, and (3) no rescaling, for cutoff values that set to zero all weights that are less than 10.00%, 5.00%, 1.00%, and 0.50% of the maximum values in the row vectors. Figure 6 shows the reconstructed images obtained after 10,000 iterations using the different algorithms and the thresholded weight matrices after rescaling the maximum of each column vector to 1. Figure 7A illustrates the 2-D reconstruction results from each individual CW source for the off-axis rod case after 100,000 iterations using the three algorithms and the same matrix rescaling technique used to compute the images shown in Figure 5. Results in Figures 7B are 2-D limited reconstructed images after 100 iterations using the CGD algorithm and the matrix rescaling technique that sets the maximum value of each column vector to one, from all four or each individual TH source. Results of Figure 8 are the 2-D reconstructed images for the 13-rod case using the three algorithms and the previous rescaling technique after 100, 1,000, and 10,000 iterations from both normal and oblique CW sources, as shown in Figure 4D.

	10.00%	5.00%	1.00%	0.50%	0.10%
Rescaling Max to 1	40,928	35,090	21,849	16,652	9,136
Rescaling Avg. to 1	30,978	24,658	13,833	10,392	4,468
No Rescaling	28,214	22,708	12,970	9,940	5,072

Table 3. Number of weight element set to zero in the weight matrix threshold titration study for the different matrix rescaling methods.

5. DISCUSSION AND CONCLUSIONS

The purpose of this study has been to examine the dependence of image quality for images computed from tomographic measurements of highly scattering media on factors related to the physical measurement and computational complexity. In practice, separation of these two parameters is never complete since invariably image quality is dependent on both. For a given algorithm, three factors of particular importance influencing the computational complexity are the volume of the medium considered, the number of elements in the weight matrix and the number of source detector pairs. Results from the volume study (Fig. 5) showed that all three types of reconstructions provided good image quality and obeys the following inequality: 3-D > 2-D ≈ 2-D limited. This indicates that, although the inverse problem in optical diffusion tomography is intrinsically 3-dimensional, because scattered photon migrate above and below the source detector plane, a 2-D reconstruction restricted to the central plane may be adequate for acceptable image quality, at least for axially symmetric problems. The time required for 2-D or 2-D limited reconstruction is much less (< 10 %) than that required for the 3-D reconstruction in this study. This saving in computation time is significant. For complex media such as tissues, it is evident that the assumption of axial symmetry will be frequently violated. However, it seems plausible that a layer-stripping scheme could be developed in which a series of 2-D slices are computed and through iterative corrections of estimated spatial convolutions, an improved 3-D reconstruction could be obtained.
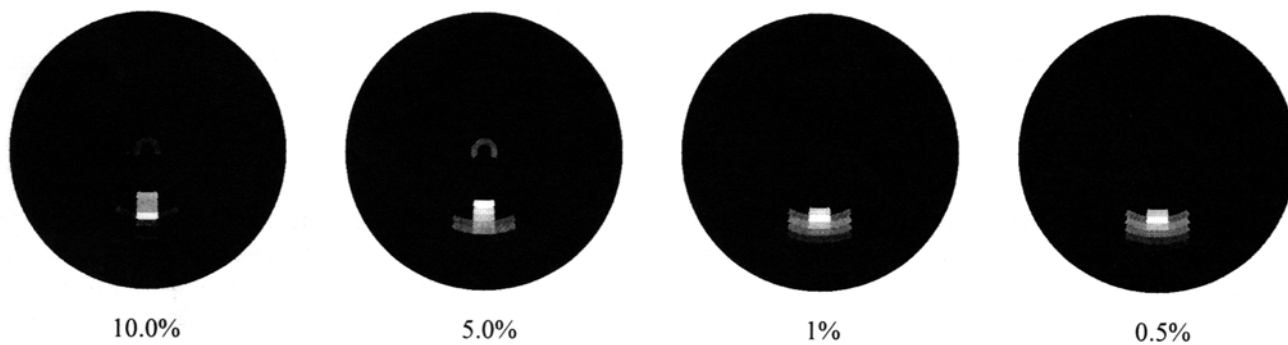
The results of the threshold titration study (Figure 6) shows that artifacts were present in the reconstruction when the threshold was 5% or higher, and no significant differences of image quality were observed when the thresholds were less than 1%. If we choose 1% as the acceptable cutoff, Table 3 shows us that up to 38% (21849/57600) of the elements in the weight matrix contain negligible information. If an algorithm could be adopted to ignore these elements during the reconstruction, this could offer a savings of up to 38% in computer time and memory. Even in the worst case (without rescaling), a 23% saving is still significant. This difference demonstrates the additional savings that can be gained by use of the matrix rescaling method [11].

Results in Figure 7 demonstrate, among others, the effect of restricting the number of source-detector pairs on image quality. Although reconstructions obtained using four source positions are improved compared to those with a single source, valuable cross-sectional information is still obtained. Interestingly, the degradation was most serious in the regions opposite the source. We believe this is due to the relatively smaller weight in those regions. Since the weight is the angular integration of the product of the forward (from the source to the voxel) and adjoint (from the detector to the voxels), those voxels farthest from both the source and detector will have the smallest weight. This will cause the weight matrix to be ill-posed and sensitive to noise, thus degrading image quality. This study shows that to get the best image

(A) POCS

10.0%   5.0%   1%   0.5%

(B) CGD

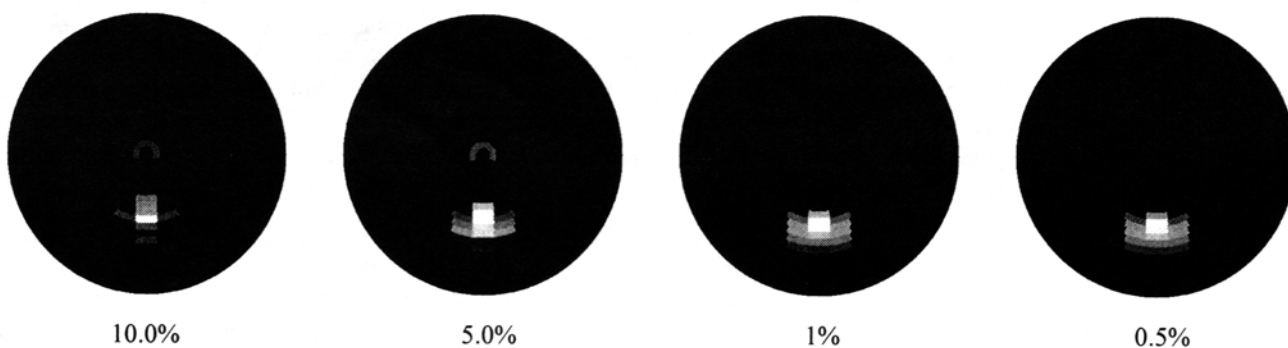10.0%   5.0%   1%   0.5%

(C) SART

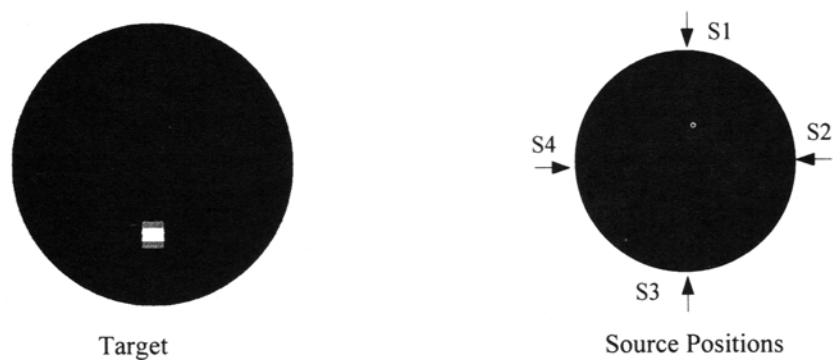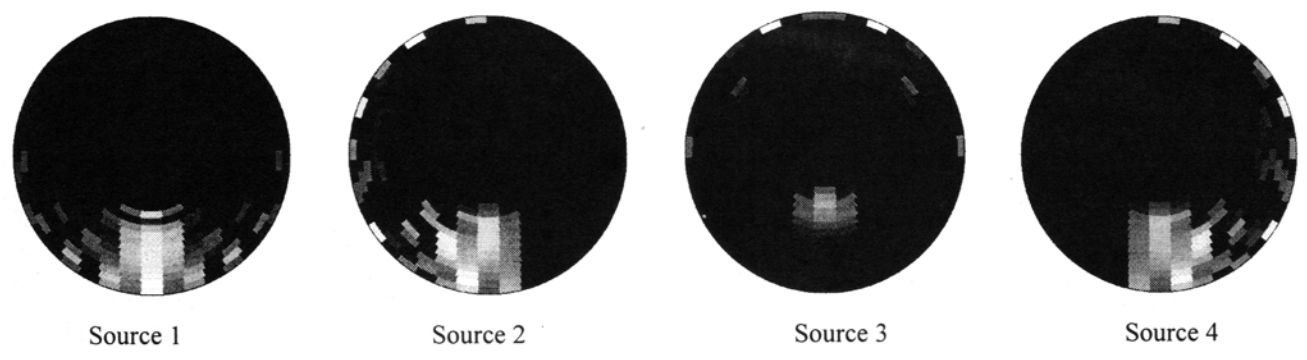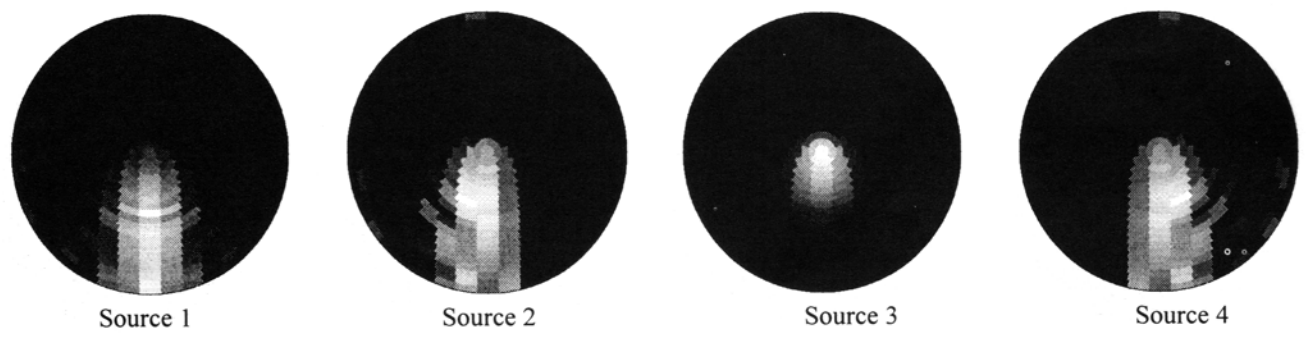10.0%   5.0%   1%   0.5%
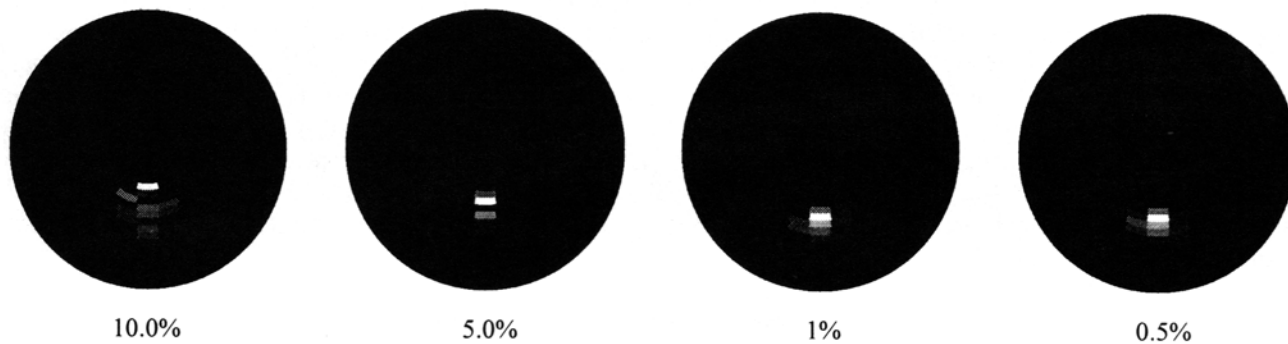
Figure 6. 2-D reconstruction results of the "threshold titration" study for the off-axis rod case after 10,000 iterations using rescaling technique (rescaling the maximum of column vector to 1) and (A) the POCS algorithm, (B) the CGD algorithm, and (C) the SART algorithm. Four cutoffs: 10.0%, 5.0%, 1.0%, and 0.5%, were used.
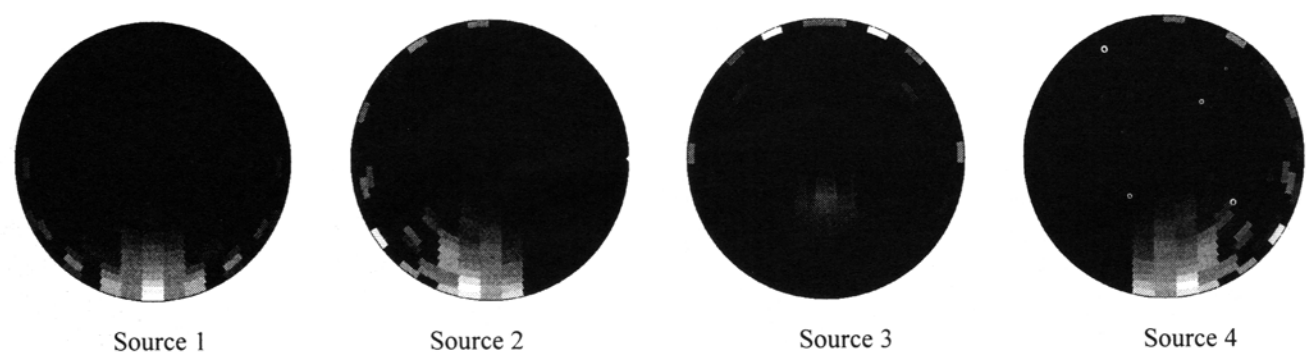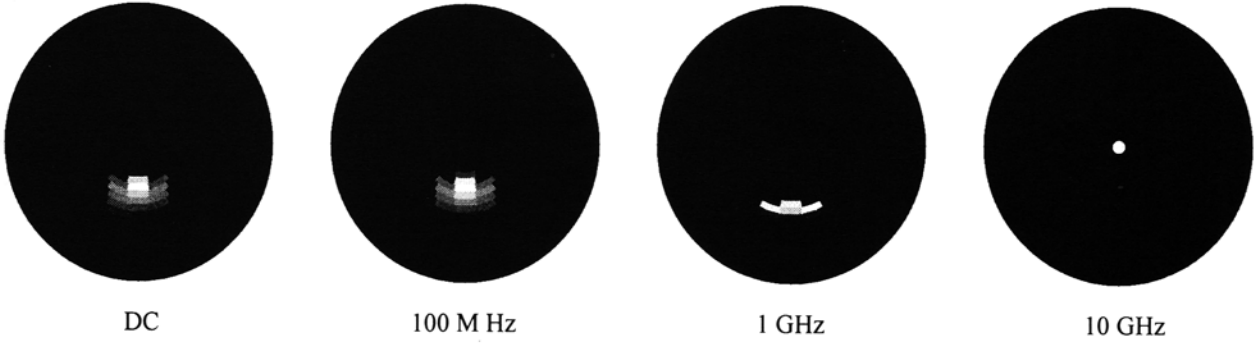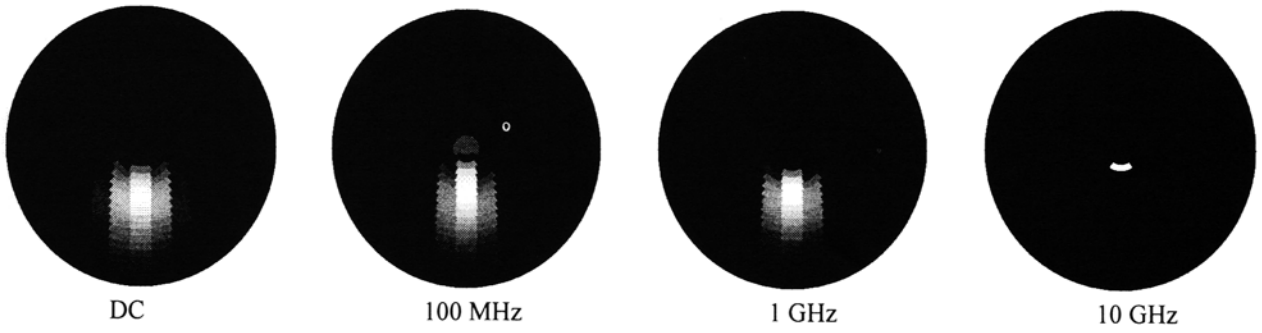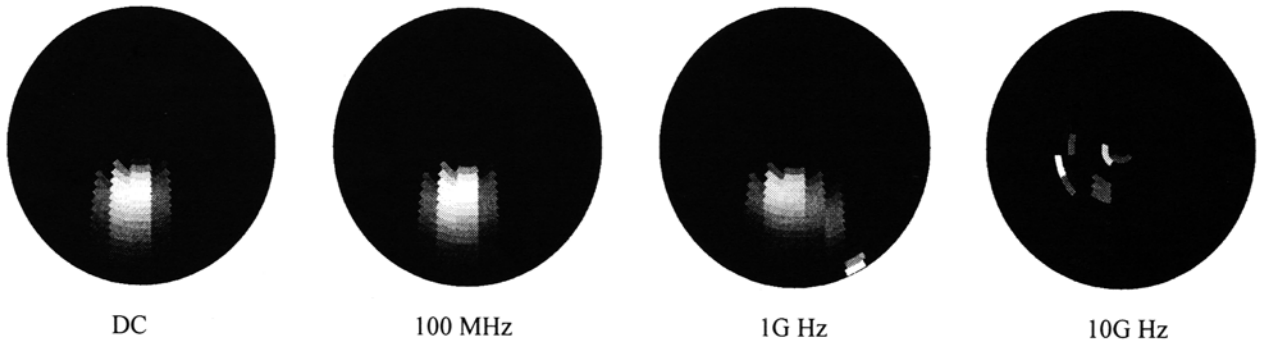
Target

Source Positions

(A) POCS

Source 1   Source 2   Source 3   Source 4

(B) CGD

Source 1   Source 2   Source 3   Source 4

(C) SART

Source 1   Source 2   Source 3   Source 4
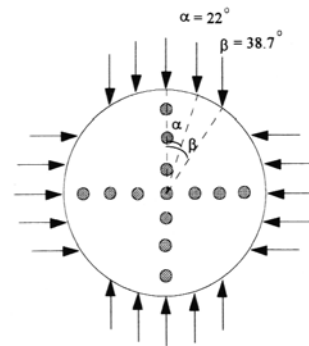
Figure 7A. 2-D reconstruction results from detector readings of each individual CW sources after 100,000 iterations using matrix rescaling technique (rescaling the maximum of each column to 1) and (A) the POCS algorithm, (B) the CGD algorithm, and (C) the SART algorithm.

All Sources

DC	100 M Hz	1 GHz	10 GHz

Source 1

| DC | 100 MHz | 1 GHz | 10 GHz |

Source 2

| DC | 100 MHz | 1G Hz | 10G Hz |

Source 3

| DC | 100 MHz | 1 GHz | 10 GHz |
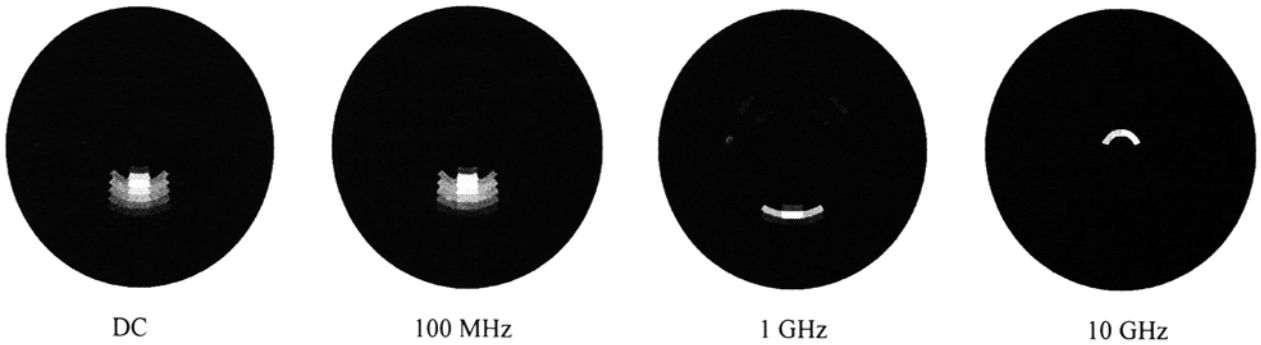
Figure 7B. 2-D limited TH reconstruction results from detector readings of all sources or each individual sources after 100 iterations using matrix rescaling technique and the CGD algorithm for four different modulated frequencies: DC, 100M Hz, 1G Hz, and 10G Hz.

Target

Source Configuration

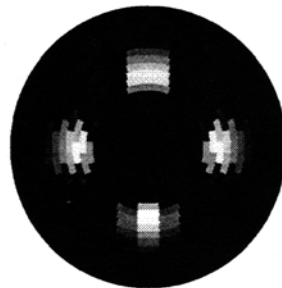$\alpha = 22^\circ$

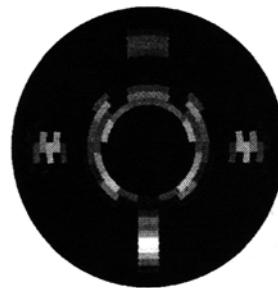$\beta = 38.7^\circ$

(A) POCS
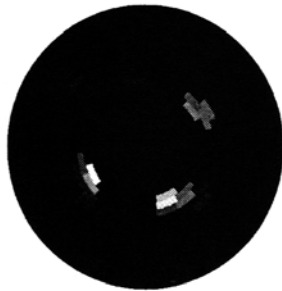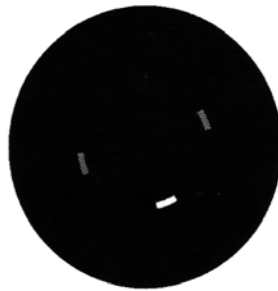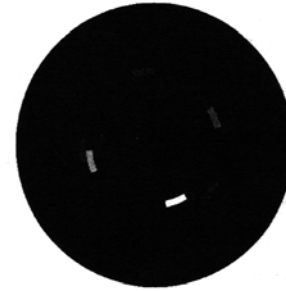
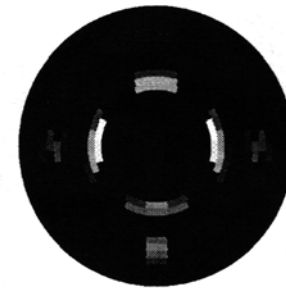100 iterations   1,000 iterations   10,000 iterations

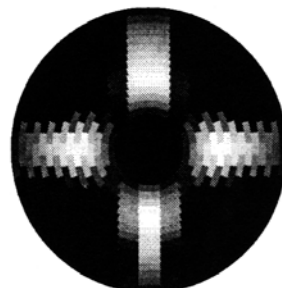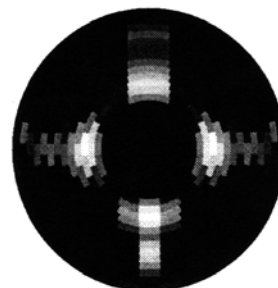(B) CGD

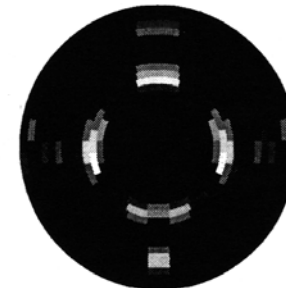100 iterations   1,000 iterations   10,000 iterations

(C) SART

100 iterations   1,000 iterations   10,000 iterations

Figure 8. 2-D reconstruction results for 13 rod case from data with both normal and oblique view angles (see sketch) using matrix rescaling technique (rescaling the maximum of each column vector to 1) and (A) the POCS algorithm, (B) the CGD algorithm, and (C) the SART algorithm.

quality, the source and detector should be uniformly distributed around the target medium. As indicated already, even in the restricted situation of a single source, useful information is still available. In fact, when compared to x-ray imaging, this result is somewhat paradoxical. This follows since, while it is evident that in the absence of scattering, a high resolution image can be obtained from a single fan-beam type projection, information about the spatial distribution of the cross-section requires multiple projections. By contrast, our results show that substantial information about the cross section can be obtained from *highly scattering media* with only a single fan-beam type projection.

Factors of particular importance regarding the physical measurement include the source condition, and selected view angle. Already discussed were the results obtained comparing single *vs.* multiple sources. Results shown in Figure 8 have examined the dependence of image quality for the 13-rod problem for a transaxial *vs.* a radial scan. The use of oblique sources was inspired by CT imaging, where parallel or fan beam source-detectors configurations are used. Results showed that improved resolution was obtained with a transaxial scanning configuration using the CGD and SART algorithms. This was achieved even though the number of source-detector pairs considered was approximately half that for the radial scan. In all cases examined, resolution of the center most region for this problem was difficult. This finding is not unexpected in view of the significant self-shielding that likely will occur, together with the fact that the weight in this region will be the smallest. To a limited extend we have also explored the influence the source condition has on image quality. In particular, we have compared the image quality obtained from a DC and time harmonic source. Results obtained for a 100 MHz modulation frequency appeared comparable to a DC source. At higher frequencies, significant changes were observed, with some suggestion of improved results at 1 GHz with multiple sources. If we look at Table 2, since the width of the impulse response of the simulated data was 500 mft, the Fourier transform is essentially DC when the frequency is below 100 MHz, which has a four times longer period than the signal width. When the frequency is between 100 MHz and 1 GHz (or the period is between 2000 mft to 200 mft), significant phase and amplitude differences will occur and contribute different information for different frequencies. When the frequency is above 1 GHz, or the period is much smaller than the signal width, the Fourier transform will average out the signal and only noise plays a dominant role in the reconstruction.

7. REFERENCES

1. J. Chang, H. L. Graber, R. L. Barbour, "Progress toward optical mammography: imaging in dense scattering media using time-independent optical sources," *Proceedings of 1994 IEEE Medical Imaging Conference*, Norfolk, Nov. 1994.

2. H. L. Graber, J. Chang, R. Aronson, R. L. Barbour, "A perturbation model for imaging in dense scattering media: derivation and evaluation of imaging operators," in *Medical Optical Tomography: Functional Imaging and Monitoring*, SPIE Institutes vol. IS11, pp. 121-143, SPIE Press, 1993.

3. R. L. Barbour, H. L. Graber, Y. Wang, J. Chang, and R. Aronson, "A Perturbation Approach for Optical Diffusion Topography Using Continuous-Wave and Time-Resolved Data," in *Medical Optical Tomography: Functional Imaging and Monitoring*, SPIE Institutes vol. IS11, pp. 87-120, SPIE Press, 1993.

4. K. M. Case, P. F. Zweifel, *Linear Transport Theory*, Addison–Wesley, Reading, MA , 1967.

5. A. Ishimaru, *Wave Propagation and Scattering in Random Media*, Academic Press, NY, 1978.

6. D. C. Youla, "Mathematical theory of image reconstruction by the method of convex projections," *Image Recovery : Theory and Application*, Henry Stark, ed., Academic Press, New York, 1987.

7. P. E. Gill, W. Murray, and M. H. Wright, *Practical Optimization*, Academic Press, New York, 1981.

8. G. Strang, *Introduction to Applied Mathematics*, Wellesley-Cambridge Press, MA, 1986.

9. A. C. Kak and M. Slaney, *Principles of Computerized Tomographic Imaging*, IEEE Press, New York, 1988.

10. A. H. Anderson and A. C. Kak, "Simultaneous Algebraic Reconstruction Technique (SART): a Superior Implementation of the ART Algorithm." *Ultrasonic Imaging*, vol. 6, pp. 81-94, 1984.

11. J. Chang, H. L. Graber, R. L. Barbour, "Image reconstruction of dense scattering media from CW sources using constrained CGD and a matrix rescaling technique," see accompanying paper in this proceedings.